

Effect of Thickness on Degradation of Austenitic 347H Steel by Direct-fired Supercritical CO₂ Power Cycle Environment

Sajedur R. Akanda¹, Richard P. Oleksak^{1,2,*}, Reyixiati Repukaiti^{1,3}, Kyle A. Rozman^{1,2}, Ömer N. Doğan^{1,*}

1-National Energy Technology Laboratory, 1450 Queen Ave SW, Albany, OR, 97321, USA

2-NETL Support Contractor, 1450 Queen Ave SW, Albany, OR, 97321, USA

3-School of Mechanical, Industrial, and Manufacturing Engineering, Oregon State University, Corvallis, OR, 97331, USA

*Corresponding Authors:

Richard.Oleksak@netl.doe.gov

Omer.Dogan@netl.doe.gov

Abstract

Austenitic 347H steel of two thicknesses (2.54 and 0.6 mm) was exposed to a simulated direct-fired supercritical CO₂ (sCO₂) power cycle environment at 650°C and 1 atm for 1000 h then tensile stressed at room temperature to study the deformation behavior.

The thicker 347H formed a protective chromia scale over most of the surface, which minimized carburization of the underlying steel and resulted in no change in mechanical performance. In stark contrast, the thinner 347H formed non-protective Fe-rich oxides over the entire surface, resulting in extensive carburization of the underlying steel. This led to increased strength but significantly reduced ductility, resulting in partially brittle failure.

Keywords: (A) stainless steel; (C) carburization; (C) oxidation; (C) hardening; supercritical CO₂ power cycle; mechanical behavior

1. Introduction

18Cr-8Ni austenitic stainless steels (Type 304, 316, 347, etc.) are potential candidates for supercritical CO₂ (sCO₂) power cycle components due to a favorable combination of high temperature strength, oxidation resistance, and cost. In particular, the oxidation resistance is achieved by formation of a slow-growing, protective chromia scale (note that “chromia” is used in the general sense to refer to a Cr-rich oxide and not necessarily pure Cr₂O₃ with corundum structure) during exposure to many high temperature environments. If this type of scale does not form (or if it fails), much faster Fe-rich oxide growth ensues, leading to more rapid recession of the metallic (load-bearing) section of the component and therefore a shorter lifetime [1].

Environments containing high levels of CO₂ present an additional concern: the possible transfer of carbon into the steel substrate during the exposure, i.e., carburization, which can significantly affect the mechanical properties of the steel [2]. It is well known that Fe-rich oxide scales are considerably more permeable to carbon than chromia scales [3]. Hence, both faster rates of surface oxidation and steel carburization are expected in the absence of a protective chromia scale.

From the above, it is clear that the oxidation resistance of Fe-Cr based steels in high temperature CO₂ is largely a question of whether a chromia-scale is formed and maintained during the exposure. Steel thickness can play an important role in determining this. When the oxide layer grows, the steel substrate bends to accommodate growth stress. From Stoney's equation, with the reduction of substrate thickness the curvature of the substrate may increase to a level which can cause fracture of oxide scale during oxide growth [4, 5]. Furthermore, thinner samples contain

a smaller reservoir of Cr and other elements important for oxidation in order to re-form this protective layer in the event of scale failure [6, 7].

Impurities such as H₂O and O₂ present in a direct-fired CO₂-rich stream [8] can also influence the ability of the steel to form and maintain a protective chromia scale [9]. The effect of these impurity additions appears to be a multifaceted, complex function of gas composition, temperature, etc. Indeed, instances of beneficial, detrimental, or negligible effects of H₂O, O₂, or combinations thereof have been reported for various chromia-forming alloys exposed to high-temperature CO₂-rich environments [10-16]. From a practical perspective, this highlights the need to test candidate steels in environments which, as closely as possible, simulate the expected conditions of the application.

It is anticipated that a major consequence of simultaneous surface oxidation and substrate carburization of a steel is the degradation of its mechanical properties such as reduction of ductility, which can lead to an unexpected failure of a component during sCO₂ power cycle operation. Previously, Pint et al. performed room temperature tensile testing on different alloys exposed to 1-300 bar and 750°C CO₂ environments but observed no degradation of mechanical properties after 500h exposure [17].

Alternatively, mechanical degradation in the form of loss in ductility has been observed in various austenitic stainless steels exposed to pure CO₂ at temperatures of 550-750°C and pressures of 1-200 bar, which was attributed to the formation of metal carbides in the alloy matrix [18-20].

In the present study, 347H steel of two thicknesses (2.54 mm and 0.6 mm) was exposed to a simulated direct-fired sCO₂ power cycle environment and then tensile tested at room temperature to study the resulting degradation of mechanical properties.

The exposed samples were cross-sectioned and characterized using Vickers hardness tests and a variety of other techniques to analyze the internal oxidized and carburized zones. The correlated data enabled understanding the role of the different zones on the overall deformation of the exposed 347H [21].

2. Experimental Details

Tensile test specimens were machined from 25.4 mm thick 347H steel plate. The plate was manufactured by Outokumpu Stainless Plate, LLC. The chemical composition of the steel plate provided by its manufacturer are listed in Table 1. The 347H plate underwent solution annealing at 1065°C followed by a water-quench by the manufacturer. Details of the design and machining of the tensile specimens can be found in the reference [22].

The detailed exposure process was described previously [22]. In short, the tensile specimens were inserted into a ceramic tube furnace and then exposed at 650°C and 1 atm for 1000h to a gas that simulated the composition of a direct-fired sCO₂ power cycle environment. The gas consisted of a mixture of 95 vol% CO₂, 1 vol% O₂ and 4 vol% H₂O (henceforth referred to as “DF4”). An additional set of tensile specimens were exposed to vacuum (10⁻⁶ torr) at 650°C for 1000h.

To obtain the mass change due to the formation of internal zones, each tensile specimen was weighed before and after the exposure using a microbalance with 0.01 mg resolution. After the exposure, each exposed specimen was tensile tested at room temperature. From the test results, mechanical properties such as 0.2% yield stress, ultimate tensile strength (UTS), % area reduction (ductility) and toughness which is

defined as the area under stress-strain curve were determined for each specimen. The details of the tensile testing were described previously [22].

To perform microstructural analyses, cross-sections were cut out from the grip sections of the exposed tensile specimens and then polished to a 0.05 μm colloidal silica finish. The cross-sections were imaged by scanning electron microscopy (SEM) using an FEI Inspect F50 operating at 5 kV or 20 kV. Vickers micro-hardness tests were performed along the cross-sections at room temperature by applying 500 g load using a Buehler MicroMet II hardness tester.

The amount of carbon uptake by the specimens during the exposure was obtained by combustion analysis of the specimens in LECO system (CSLLL4S) using NIST certified standards. Phase analysis was performed by X-ray diffraction (XRD) using a Rigaku D/Max 2200PC Ultima III using $\text{Cu K}\alpha$.

3. Results

3.1 Degradation of Mechanical Properties of 2.54 mm and 0.6 mm Thick 347H

Figure 1 presents the average mass change of three specimens each of 2.54 mm and 0.6 mm thick 347H after exposure to the vacuum and DF4 environments. The negligible mass change in each specimen after isothermal vacuum exposure confirms that the specimens were not significantly oxidized. Hence, only heating at 650°C without oxidation affected the mechanical properties during the vacuum exposure.

In the case of DF4 exposure, the thicker specimen exhibited a notable mass gain, while the thinner specimen showed a considerable mass loss. Figure 2 shows photographs of a typical 0.6 mm and 2.54 mm thick specimen after the DF4 exposure. The dark appearance of the 0.6 mm specimen indicates that the entire surface had oxidized

extensively. In addition, significant spallation was evident, consistent with the mass loss described above. Alternatively, the 2.54 mm specimen appeared only slightly discolored across most of the surface, implying a thin oxide scale, whereas regions of thicker oxide also formed on portions of the specimen. Importantly, the thick oxide only formed on the grip section of the specimen, whereas the gage section appeared to be covered exclusively by a thin oxide.

Figure 3 presents representative engineering stress-strain curves of the 0.6 mm and 2.54 mm thick 347H tensile specimens before and after the exposures. All the specimens failed in ductile mode. The mechanical properties obtained from all of the tests are summarized in Table 2. Fig. 4(a) compares the as-received (AR) and the vacuum exposed results to assess the effect of 650°C isothermal exposure on the mechanical properties. For the 2.54 mm thick 347H, the mechanical properties were not significantly affected. However, for the 0.6 mm thick 347H, the toughness was found to decrease by ~20%.

Figure 4(b) compares the DF4 and vacuum exposed results. It is clear that the 2.54 mm thick 347H was essentially unaffected by the DF4 exposure. Alternatively, the 0.6 mm thick 347H specimen was severely affected. The specimen exhibited a sizable increase in strength, both in terms of UTS (~20%) and yield stress (~100%). However, this was accompanied by a significant reduction in ductility (~80% drop in area reduction), such that the toughness of the specimen was also severely reduced (~80%).

3.2 Microstructure of DF4-exposed 2.54 mm Thick 347H

Figure 5 shows a cross-sectional SEM image and corresponding EDS maps of the 2.54 mm thick DF4-exposed specimen. The majority of the surface was characterized by a

thin ($< 1 \mu\text{m}$) chromia scale, as shown in Fig. 5a-b. However, a smaller portion of the surface was covered by a much thicker, Fe-rich oxide scale as shown in Fig. 5c-d. This chromia scale, which formed over most of the surface including the entire gage section of the specimen (Fig. 2), prevented any significant amount of carburization of the underlying steel substrate [9]. This resulted in similar mechanical behavior of 2.54 mm thick 347H exposed to DF4 compared to the vacuum exposed specimen.

3.3 Microstructure of DF4-exposed 0.6 mm Thick 347H

Figure 6 shows a cross-sectional SEM image and corresponding EDS maps of the 0.6 mm thick DF4-exposed specimen. The results reveal a non-uniform oxidation front that has reached a depth of $\approx 60 \mu\text{m}$ into the alloy. The appearance of this oxidized region is very similar to the inner oxide layer identified on the 2.54 mm thick specimen, in regions that experienced chromia failure (Fig. 5c-d). Indeed, the EDS mapping in Fig. 6 confirms Fe, Cr, and Ni in the oxide, consistent with the inner oxide in Fig. 5c-d, while remnants of an Fe-oxide outer layer are also seen in Fig. 6c. This implies that the outer oxide had spalled for the 0.6 mm thick specimen, which was the case for the entire cross-section. Scale spallation induced by thermal cycling is a well-known problem for austenitic steels, owing to the very large difference in thermal expansion coefficients of the oxide scale and steel substrate. Furthermore, spallation often occurs at the interface of the inner and outer oxide layers (i.e., the original steel surface) [3]. XRD analysis (not shown) of the DF4-exposed 0.6 mm thick specimen on regions both with and without severe oxide spallation (as defined in Fig. 2) indicated exclusively M_3O_4 structure in all cases. Thus, the 0.6 mm thick 347H formed a duplex oxide structure consisting of an outer layer of essentially pure Fe_3O_4 (magnetite) and inner layer of M_3O_4 spinel oxide (M

= Fe, Cr, Ni), where the outer Fe_3O_4 layer spalled, likely during cooling at the end of the exposure, resulting in the relatively large mass loss ($-6.3 \pm 3.2 \text{ mg/cm}^2$) shown in Fig. 1.

The LECO (combustion) analysis indicated a bulk carbon content of the 0.6 mm specimen of $\sim 0.53 \text{ wt.}\%$, which is ~ 10 times the amount present before exposure (Table 1). This result indicates that along with oxidation, the 0.6 mm thick 347H experienced severe carburization during the DF4 exposure. To understand the distribution of carbon, a microprobe line scan was collected across the 0.6 mm thick 347H as shown in Fig. 7. The profile reveals an extremely large quantity (4-6 wt%) of carbon. This is unrealistically high, considering that Fe_3C (cementite) is 6.7% carbon by weight. The reason for this overestimation may be due to carbon deposition from the electron beam during the analysis. Nevertheless, the line scan reveals a distribution of carbon that suggests diffusion into the material, where the carbon level at the oxide/alloy interface is approximately 0.5 wt% higher than that at the center of the specimen.

The carburized state of the 0.6 mm thick 347H was further evaluated by etching the specimen cross-section, as shown in Fig. 7. The low magnification image in Fig. 7(a) reveals extensive intergranular carbides throughout the entire specimen thickness. Higher magnification images taken immediately below the inner oxide layer (Fig. 7(b)) and at the middle of the specimen (Fig. 7(c)) show that the density of grain boundary carbides is approximately the same throughout the entire specimen. These images also show that a relatively high concentration of smaller, intragranular carbides formed within a zone that extended approximately $2 \mu\text{m}$ from the grain boundaries, both at the surface and the middle of the specimen. Finally, even smaller intragranular carbides are also observed further from the boundaries, in the grain interiors. Close inspection reveals

that these carbides were present at higher concentration near the surface of the specimen (Fig. 7(b)) compared to the middle of the specimen (Fig. 7(c)).

To further characterize the microstructure of the DF4-exposed 0.6 mm thick 347H specimen, XRD was performed after removing the surface oxide by mechanical grinding and the results are shown in Fig. 9. Large peaks are seen for both FCC and BCC alloy phases. The presence of significant BCC phase can be explained by the grinding process, which is known to produce a surface layer of BCC (or BCT) grains on 347H, which has a metastable FCC structure, via mechanically induced martensitic transformation [23]. In addition, it is possible that some FCC to BCC conversion occurred by the depletion of metallic Cr from the matrix accompanying carbide formation throughout the specimen, as the FCC phase stability region narrows when Cr content is lowered in the Fe-Cr-Ni ternary system. Small but measurable peaks are also seen in Fig. 9 corresponding to Cr_{23}C_6 , indicating the presence of Cr-rich M_{23}C_6 carbides.

4. Discussion

4.1 Oxidation and Carburization Mechanisms

The oxidation behavior of Fe-Cr based steels in high temperature CO_2 -rich environments can largely be separated into three regimes, which are influenced by Cr content, temperature, and other factors: (1) slow parabolic growth of a chromia scale (2) fast parabolic growth of an Fe-rich duplex oxide scale (3) faster linear growth of Fe-oxide, also known as breakaway oxidation [1]. Regime 1 is associated with only minimal carburization of the underlying steel, since chromia scales have very limited permeability for carbon [3]. The results show that 2.54 mm thick 347H oxidized within

this regime for a significant portion of the specimen surface, which led to only a very small fraction of the specimen thickness that was affected by oxidation or carburization. This is consistent with prior studies of relatively thick 347H exposed to the same environment at somewhat lower temperature of 550°C [9]. Consequently, the mechanical properties were similar to those of the vacuum exposed specimen.

The 0.6 mm thick 347H behaved completely differently. The entire surface failed to passivate by chromia formation and instead entered regime 2, characterized by Fe-rich duplex oxide growth as described in Section 3.3. Steels that contain relatively high levels of Cr (~15-20 wt%) can often “recover” from Fe-rich duplex oxide growth by the formation of a continuous chromia layer at the base of the scale, thereby reducing the oxidation rate once again to that which is controlled by chromia growth [24]. Indeed, this is seen to limit penetration of the inward-growing oxides that formed occasionally on the 2.54 mm thick 347H, as shown in Fig. 5c. Evidence for the beginnings of this process is also observable for the 0.6 mm thick 347H in Fig. 6. That is, portions of the inward growing oxidation front were halted wherever a chromia layer was formed, for example near the right side of the image shown in Fig. 6. However, this layer was non-continuous, as evidenced by the regions of deepest oxidation near the left side of the image. Hence, while the 2.54 mm thick specimen was able to frequently “recover” from failure of the chromia scale, the 0.6 mm thick specimen failed to do so, resulting in Fe-rich duplex oxide growth over the entire surface.

Compared to the chromia scale formed on most of the surface of the 2.54 mm thick 347H, the Fe-rich oxide scale formed on the 0.6 mm thick 347H is significantly more permeable to carbon [3]. While there have been relatively few studies on the

mechanism of carburization for austenitic steels in high temperature CO₂ environments, extensive research has been directed toward understanding this process in 9-12Cr ferritic-martensitic steels [12, 25-27]. Since those steels form similar Fe-rich duplex oxide scales, it is reasonable to postulate that the mechanism of steel carburization may also be similar, which is as follows: The outer Fe₃O₄ layer (which completely spalled in this study) grew outward relative to the original alloy surface, by the diffusion of Fe cations from the oxide/alloy interface to the oxide surface. Meanwhile, CO₂ molecules transported through the oxide, to reach the oxide/alloy interface and supply oxygen to support growth of the inward-growing, inner oxide layer via the reaction CO₂ + M = CO + MO. The nature of CO₂ transport through the oxide is subject to debate, and elucidating the details of this process is beyond the scope of this study [3]. The CO produced at the oxide/alloy interface then either contributed to further oxide growth by direct reaction with the steel (CO + M = MO + C) or recombined via the Boudouard reaction (2CO = CO₂ + C). Regardless of the precise mechanism, this results in a very high carbon activity at the oxide/alloy interface, which drives carbon diffusion into the bulk of the steel [28]. The presence of H₂O and O₂ in the reaction gas may both serve to reduce the amount of CO₂ transport through the Fe-rich oxide scale {Oleksak, 2020 #767}, however any such reduction was apparently not sufficient to prevent significant carbon uptake.

Upon diffusing into the steel, carbon preferentially reacts with metallic Cr to form Cr-rich M₂₃C₆ carbides in 9-12Cr steels [29]. The same appears to have occurred here for the 0.6 mm thick 347H sample, where both inter- and intra-granular carbides are evident

throughout the entire specimen (Fig. 7) and $M_{23}C_6$ was the only carbide phase identified by XRD (Fig. 9).

Despite the apparent similarities in behavior of 347H during Fe-rich duplex oxide growth (described herein) compared to much prior work of 9-12Cr ferritic/martensitic steels in CO_2 -rich environments at similar temperatures {Oleksak, 2021 #935}, there are also some important distinctions. Specifically, carburization in 9-12Cr ferritic/martensitic steels occurs rather uniformly, such that a “zone” of carburization forms to a certain depth beneath the oxide scale {Oleksak, 2020 #790}. Alternatively, carburization in 347H occurred primarily along grain boundaries or in very close proximity to the grain boundaries. There are two likely reasons for this. First, carbon diffusivity is lower in an FCC matrix (347H) compared to BCC/BCT matrix (9-12Cr steels). This may also be exacerbated by the presence of a high density of fast diffusion paths in the 9-12Cr steels, such as martensite lath boundaries and prior austenite grain boundaries {Oleksak, 2021 #935}. Second, Cr-carbides become less thermodynamically stable with increasing Ni content in Fe-Cr-Ni alloys, meaning that carbon must travel on average further into the alloy before reaching a Cr content sufficient to precipitate carbide {Olivares, 2016 #564}. Collectively, this results in carbide formation in the austenitic 347H steel that occurs primarily along (or near) the grain boundaries. Importantly, this results to a certain extent in strengthening of the austenitic 347H steel, albeit with a reduction in ductility (Fig. 3). This strengthening is consistent with much earlier studies of similar 18Cr-8Ni austenitic steels in high-temperature CO_2 {Martin, 1963 #750}. Alternatively, no strengthening occurs for 9-12Cr ferritic/martensitic steels, where alloy carburization results only in embrittlement {Akanda, 2021 #877}.

The reason that 0.6 mm thick 347H failed to passivate by chromia formation when the thicker 347H succeeded is of significant technological interest, since metal sections of the order of this thickness are expected for compact heat exchangers in sCO₂ power cycles. Previous studies on the effect of specimen thickness on oxidation of Fe-Cr steels have highlighted the importance of the “reservoir” of Cr (and other minor elements important to oxidation resistance such as Si and Mn) [6]. Thus, if the depletion profiles for these elements reach the middle of the specimen, their supply to the surface will be reduced during further oxidation. However, 650°C and 1000h is a relatively low temperature and time for this to occur. Indeed, Fig. 5b shows that Cr depletion had only reached a depth of 5 μm into the alloy for regions that formed a Cr-rich oxide scale. Furthermore, Fig. 5b shows that the concentration of Cr at the oxide/alloy interface is on the order of 10 wt%, significantly higher than would be required for chemical-induced failure of the chromia scale {Evans, 1999 #595}{Nguyen, 2017 #740}. An alternative explanation is that the observed thickness effect is related to carburization of the steel. As described above, the carbon reacts to form Cr-rich carbides. This reduces the flux of metallic Cr toward the oxidation front, an effect which is more pronounced for the thinner sample. This in turn would make it more difficult for the thinner alloy to “recover” after one or more instances of failure of the chromia scale. Still, this does not explain why the chromia scale on the thinner specimen failed in the first place, as the majority of the 2.54 mm thick 347H surface never experienced chromia failure. This points to the possibility that the thicker specimen was better able to accommodate oxide growth stresses and therefore retain the originally formed chromia scale, compared to the thinner specimen [4, 5].

4.2 Failure Mode Analysis of DF4-exposed 0.6 mm Thick 347H

Figure 10 shows the hardness profile along the entire thickness of a 0.6 mm 347H specimen after the DF4 exposure. The hardness profile of a 2.54 mm specimen after DF4 exposure is also included for comparison. In the figure it is seen that, the carburized steel substrate in the 0.6 mm thick 347H is notably harder compared to the un-carburized 2.54 mm thick 347H. In particular, the inner oxide layers and their adjacent regions of the thinner 347H are significantly harder. The higher hardness of the thinner 347H suggests that this specimen has higher resistance to plastic deformation. An SEM image of the tensile fracture surface of this specimen presented in Fig. 11 reveals that the inner oxide layers near the edges had brittle fracture morphology whereas the rest of the region (carburized zone) had somewhat ductile fracture. The combination of the brittle and ductile fracture surfaces shown in Fig. 11 is consistent with the hardness profile of the thinner specimen shown in Fig. 10.

From Fig. 10 and 9, it is realized that the development of the harder internal zones resulted in reduction of ductility but increase of yield stress of the 0.6 mm thick 347H by DF4 exposure (Fig. 4(b)). Furthermore, the thicker and harder carburized zone is believed to cause the increase of UTS of this specimen. Overall, the combination of ductility reduction and UTS increase was such that the toughness of this specimen was significantly reduced.

5. Conclusion

In this study, the degradation of mechanical properties of 347H steel exposed to CO₂-rich gas with 4%H₂O and 1%O₂ at 650°C and atmospheric pressure for 1000h was investigated. Two different thicknesses of 347H were considered: 2.54 mm and 0.6 mm. The mechanical properties of the thicker 347H were found to be unaffected by the CO₂-

rich exposure, where the steel primarily formed a thin protective chromia scale that significantly limited both oxidation and carburization. Alternatively, the thinner 347H formed Fe-rich oxide layers that consumed a significant fraction (~20%) of the specimen and allowed significant carbon ingress into the steel. Both the surface oxide and the carburized steel exhibited increased hardness, which resulted in increased strength but significantly decreased ductility (~80%) and toughness (~80%). This amounts to a considerable extent of degradation from an application perspective, which suggests that caution is needed when considering 347H and similar 18Cr-8Ni steels for thin sectioned components compatible with CO₂-rich environments at temperatures close to 650°C.

Declaration of Interest

None.

Acknowledgements and Disclaimer

This work was performed by support of the U.S. Department of Energy's Fossil Energy Crosscutting Technology Research Program. The Research was executed through the National Energy Technology Laboratory's Research and Innovation Center's Advanced Alloy Development Field Work Proposal. This research was supported in part by appointments (SRA and RR) to the National Energy Technology Laboratory Research Participation Program sponsored by the U.S. Department of Energy and administered by the Oak Ridge Institute for Science and Education (ORISE). The authors like to acknowledge Trevor Godell (NETL) for machining tensile specimens, Christopher Powell (NETL) for conducting tensile tests, Matthew B. Fortner (NETL) for preparing specimen surfaces for microstructural analyses and Richard E. Chinn (NETL) for conducting XRD analyses. Joseph H. Tylczak (NETL) performed environmental exposure and Casey S. Carney (NETL) performed vacuum exposure of the tensile specimens.

This report was prepared as an account of work sponsored by an agency of the United States Government. Neither the United States Government nor any agency thereof, nor any of their employees, makes any warranty, express or implied, or assumes any legal liability or responsibility for the accuracy, completeness, or usefulness of any information, apparatus, product, or process disclosed, or represents that its use would not infringe privately owned rights. Reference herein to any specific commercial product, process, or service by trade name, trademark, manufacturer, or otherwise does

not necessarily constitute or imply its endorsement, recommendation, or favoring by the United States Government or any agency thereof. The views and opinions of authors expressed herein do not necessarily state or reflect those of the United States Government or any agency thereof.

Data availability

All relevant data that support this study are available from the corresponding author upon request.

References

- [1] R.P. Oleksak, F. Rouillard, Materials Performance in CO₂ and Supercritical CO₂, in: R.J.M. Konings, R.E. Stoller (Eds.), *Comprehensive Nuclear Materials*, Oxford, 4 (2020) pp. 422-451. <https://doi.org/10.1016/B978-0-12-803581-8.11622-4>.
- [2] H.J. Grabke, *Carburization: a high temperature corrosion phenomenon*, MTI Publication No. 52, Materials Technology Institute of the Chemical Process Industries, 1998, St. Louis, MO.
- [3] D.J. Young, *High temperature oxidation and corrosion of metals*, 2nd Edition, Elsevier, 2016.
- [4] A. Fluri, D. Pergolesi, V. Roddatis, A. Wokaun, T. Lippert, In situ stress observation in oxide films and how tensile stress influence oxygen ion conduction, *Nat Commun.* 7 (2016) 10692. <https://doi.org/10.1038/ncomms10692>.
- [5] L. B. Freund, S. Suresh, *Thin Film Materials: Stress, Defect Formation and Surface Evolution*, Cambridge University Press, 2004.
- [6] H.E. Evans, A.T. Donaldson, T.C. Gilmour, Mechanisms of Breakaway Oxidation and Application to a Chromia-Forming Steel, *Oxid. Met.* 52 (1999) 379-402. <https://doi.org/10.1023/A:1018855914737>
- [7] P. Huczkowski, Effect of geometry and composition of Cr steels on oxide scale properties relevant for interconnector applications in Solid Oxide Fuel Cells (SOFCs), PhD Dissertation, 2007, Germany.
- [8] R.J. Allam, M.R. Palmer, G.W. Brown Jr, J. Fetvedt, D. Freed, H. Nomoto, M. Itoh, N. Okita, C. Jones Jr, High efficiency and low cost of electricity generation from fossil fuels while eliminating atmospheric emissions, including carbon dioxide, *Energy Procedia* 37 (2013) 1135-1149. <https://doi.org/10.1016/j.egypro.2013.05.211>.
- [9] R.P. Oleksak, J.H. Tylczak, G.R. Holcomb, Ö.N. Doğan, High temperature oxidation of steels in CO₂ containing impurities, *Corros. Sci.* 164 (2020) 108316. <https://doi.org/10.1016/j.corsci.2019.108316> .
- [10] N. Mu, K.Y. Jung, N.M. Yanar, G.H. Meier, F.S. Pettit, G.R. Holcomb, Water Vapor Effects on the Oxidation Behavior of Fe–Cr and Ni–Cr Alloys in Atmospheres Relevant to Oxy-fuel Combustion, *Oxid. Met.* 78 (2012) 221-237. <https://doi.org/10.1007/s11085-012-9302-x>.
- [11] Y. Ikeda, K. Nii, Mechanism of accelerated oxidation of Fe-Cr alloys in water vapor containing atmosphere, *T. Natl. Res. I. Met.* 26 (1984) 52-62. https://doi.org/10.3323/jcorr1974.31.3_156

- [12] T. Gheno, D. Monceau, J. Zhang, D.J. Young, Carburisation of ferritic Fe–Cr alloys by low carbon activity gases, *Corros. Sci.* 53 (2011) 2767-2777. <https://doi.org/10.1016/j.corsci.2011.05.013>.
- [13] W.J. Quadackers, T. Olszewski, J. Piron-Abellan, V. Shemet, L. Singheiser, Oxidation of Metallic Materials in Simulated CO₂/H₂O-rich Service Environments Relevant to an Oxyfuel Plant, *Mater. Sci. Forum* 696 (2011) 194-199.
- [14] G.H. Meier, K. Jung, N. Mu, N.M. Yanar, F.S. Pettit, J.P. Abellán, T. Olszewski, L.N. Hierro, W.J. Quadackers, G.R. Holcomb, Effect of Alloy Composition and Exposure Conditions on the Selective Oxidation Behavior of Ferritic Fe–Cr and Fe–Cr–X Alloys, *Oxid. Met.* 74 (2010) 319-340. <https://doi.org/10.1007/s11085-010-9215-5>.
- [15] B.A. Pint, J. Lemusto, M.J. Lance, J.R. Keiser, Effect of pressure and impurities on oxidation in supercritical CO₂, *Mater. Corros.* 70 (2019) 1400-1409. <https://doi.org/10.1002/maco.201810652>.
- [16] J. Mahaffey, D. Adam, A. Brittan, M. Anderson, K. Sridharan, Corrosion of alloy Haynes 230 in high temperature supercritical carbon dioxide with oxygen impurity additions, *Oxid Met* 86 (2016) 567-580. <https://doi.org/10.1007/s11085-016-9654-8>.
- [17] B.A. Pint, R.G. Brese, J.R. Keiser, Effect of pressure on supercritical CO₂ compatibility of structural alloys at 750 °C, *Mater. Corros.* 68 (2017) 151-158. <https://doi.org/10.1002/maco.201508783>.
- [18] H.J. Lee, H. Kim, S.H. Kim, C. Jang, Corrosion and carburization behavior of chromia-forming heat resistant alloys in a high-temperature supercritical-carbon dioxide environment, *Corros. Sci.* 99 (2015) 227-239. <https://doi.org/10.1016/j.corsci.2015.07.007>
- [19] H.J. Lee, G.O. Subramanian, S.H. Kim, C. Jang, Effect of pressure on the corrosion and carburization behavior of chromia-forming heat-resistant alloys in high-temperature carbon dioxide environments, *Corros. Sci.* 111 (2016) 649-658. <https://doi.org/10.1016/j.corsci.2016.06.004>.
- [20] A.M. Brittan, J.T. Mahaffey, N.E. Colgan, M. Elbakhshwan, M.H. Anderson, Carburization resistance of cu-coated stainless steel in supercritical carbon dioxide environments, *Corros. Sci.* 169 (2020) 108639. <https://doi.org/10.1016/j.corsci.2020.108639>.
- [21] D. Tabor, The Physical Meaning of Indentation and Scratch Hardness, *Br. J. Appl. Phys.*, 7 (1956) 159-166. <http://dx.doi.org/10.1088/0508-3443/7/5/301>.
- [22] S.R. Akanda, R.P. Oleksak, R. Repukaiti, K.A. Rozman, Ö.N. Doğan, Effect of Specimen Thickness on the Degradation of Mechanical Properties of Ferritic-Martensitic P91 Steel by Direct-fired Supercritical CO₂ Power Cycle Environment, *Metall Mater Trans A* 52 (2021) 82-93. <https://doi.org/10.1007/s11661-020-06065-9>.

- [23] R.P. Oleksak, G.R. Holcomb, C.S. Carney, L. Teeter, Ö.N. Doğan, Effect of Surface Finish on High-Temperature Oxidation of Steels in CO₂, Supercritical CO₂, and Air, *Oxid. Met.* 92 (2019) 525-540. <https://doi.org/10.1007/s11085-019-09938-6>.
- [24] H.E. Evans, D.A. Hilton, R.A. Holm, S.J. Webster, The development of localized pits during stainless steel oxidation, *Oxid. Met.* 14 (1980) 235-247. <https://doi.org/10.1007/BF00604566>.
- [25] F. Rouillard, G. Moine, M. Tabarant, J.C. Ruiz, Corrosion of 9Cr Steel in CO₂ at Intermediate Temperature II: Mechanism of Carburization, *Oxid. Met.* 77 (2012) 57-70. <https://doi.org/10.1007/s11085-011-9272-4>.
- [26] D. Young, P. Huczkowski, T. Olszewski, T. Huttel, L. Singheiser, W.J. Quadackers, Non-steady state carburisation of martensitic 9–12%Cr steels in CO₂ rich gases at 550°C, *Corros. Sci.* 88 (2014) 161-169. <https://doi.org/10.1016/j.corsci.2014.07.024>.
- [27] Y. Gong, D.J. Young, C. Atkinson, T. Olszewski, W.J. Quadackers, R.C. Reed, Modelling of the degradation of martensitic stainless steels by the Boudouard reaction, *Corros. Sci.* 173 (2020) 108699. <https://doi.org/10.1016/j.corsci.2020.108699>.
- [28] D.J. Young, J. Zhang, Alloy Corrosion by Hot CO₂ Gases, *JOM* 70 (2018) 1493-1501. <https://doi.org/10.1007/s11837-018-2944-7>.
- [29] Y. Gong, D.J. Young, P. Kontis, Y.L. Chiu, H. Larsson, A. Shin, J.M. Pearson, M.P. Moody, R.C. Reed, On the breakaway oxidation of Fe9Cr1Mo steel in high pressure CO₂, *Acta Materialia* 130 (2017) 361-374. <http://dx.doi.org/10.1016/j.actamat.2017.02.034>.

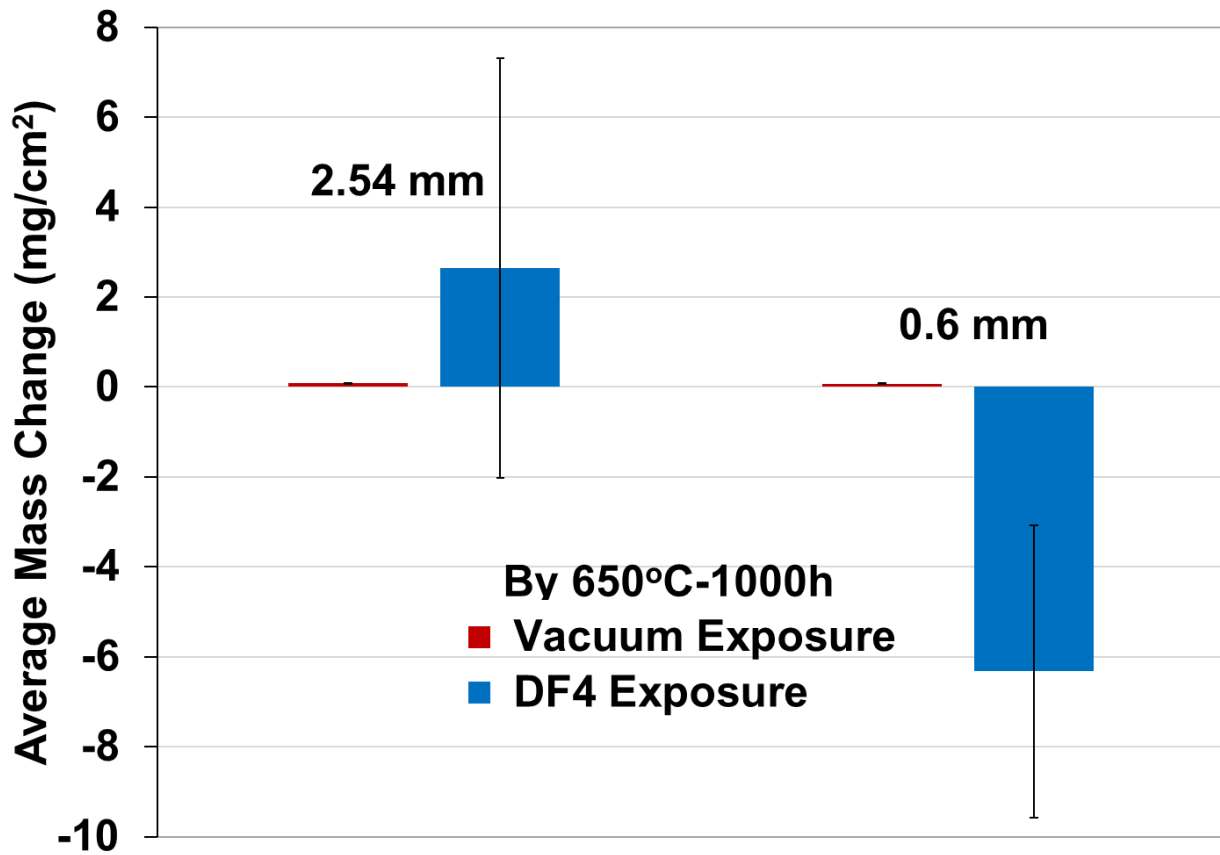


Fig. 1 Average mass change per surface area in 2.54 mm and 0.6 mm thick 347H after exposure to vacuum or DF4 at 650°C for 1000h. Error bar represents standard deviation obtained from three specimens.

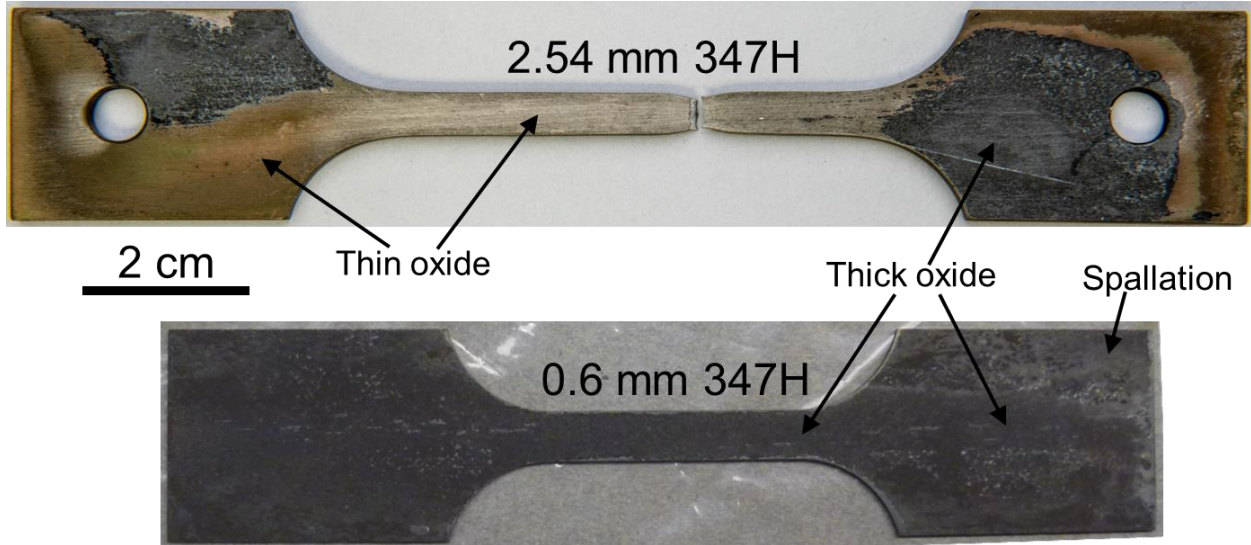


Fig. 2 Photos of a typical 2.54 mm (thick) and 0.6 mm (thin) 347H specimen after the DF4 exposure. Note that the thick specimen had been tensile tested prior to the photo and is therefore elongated and fractured.

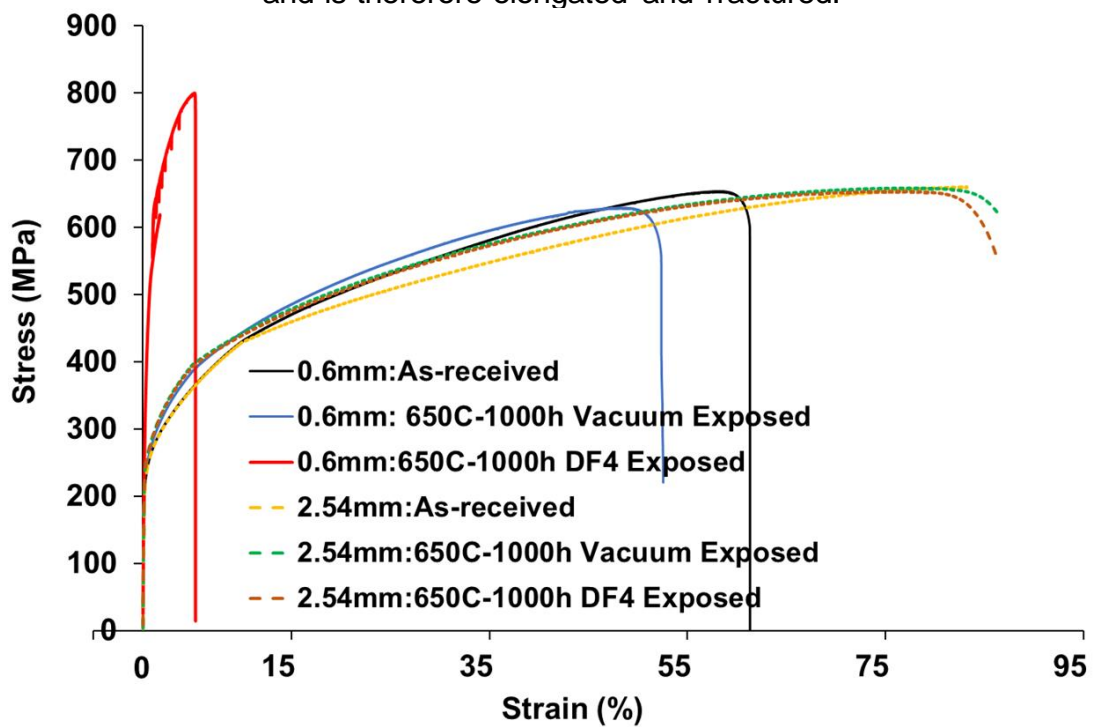
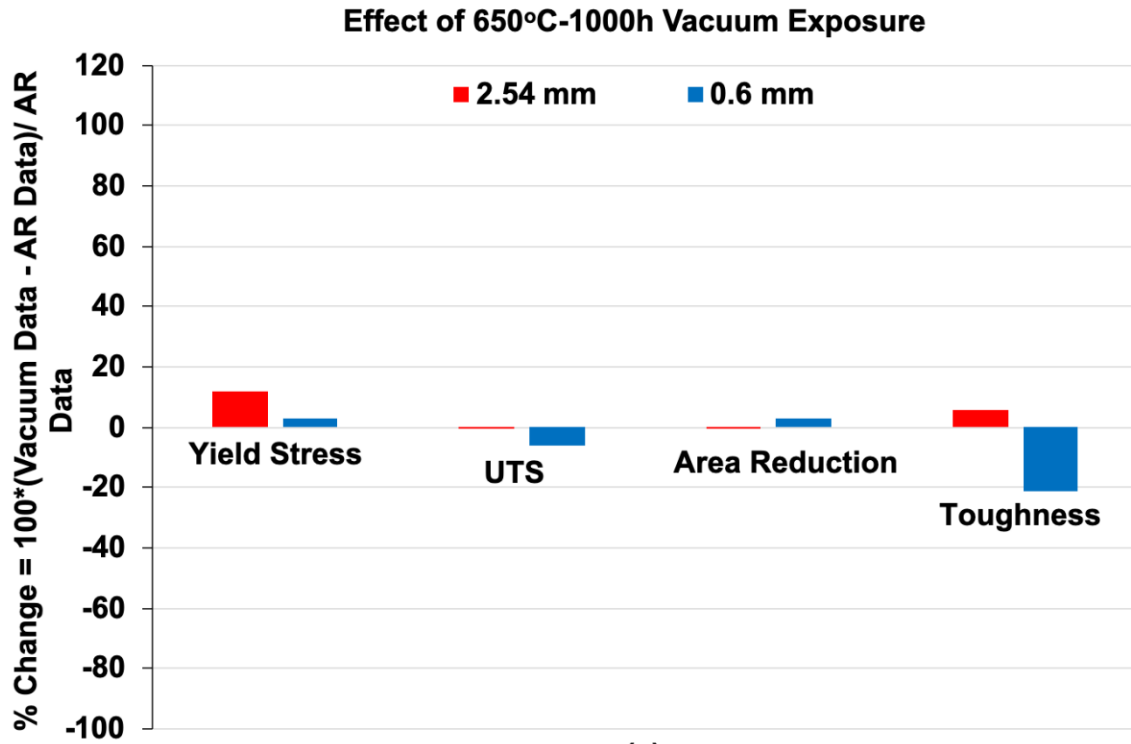
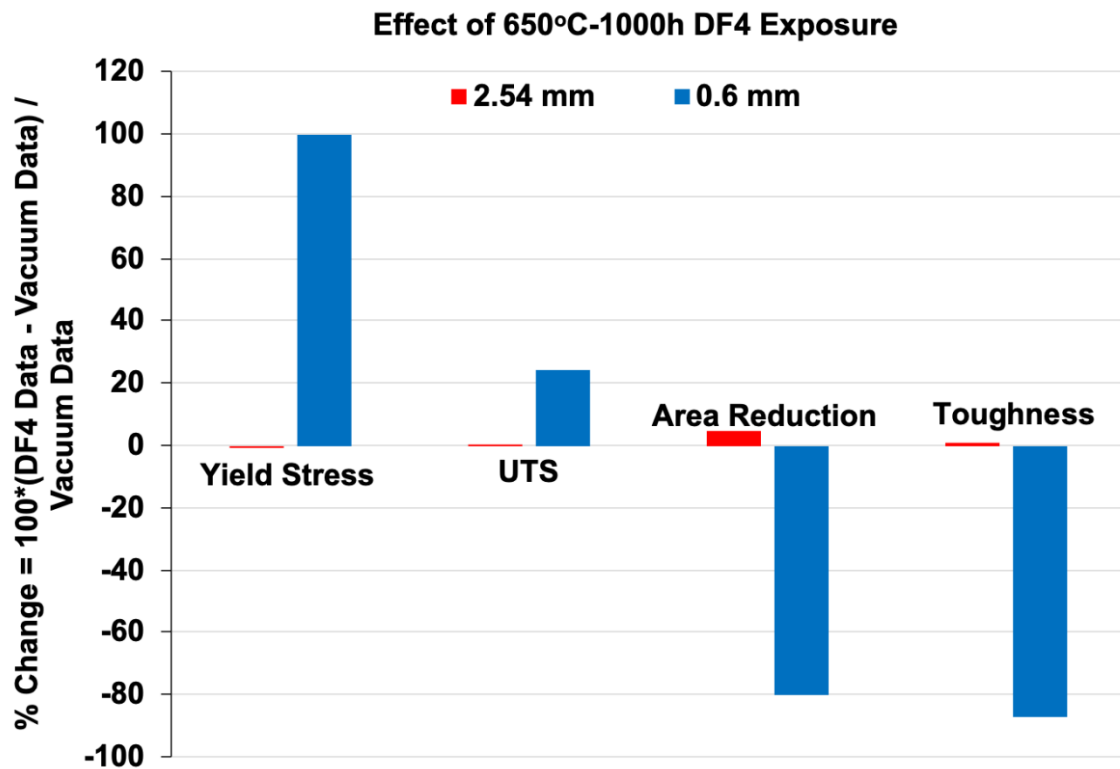


Fig. 3 Engineering stress-strain curves obtained from room temperature tensile testing on as-received, 650°C-1000h vacuum and 650°C-1000h DF4-exposed 347H specimens.



(a)



(b)

Fig. 4 Change of mechanical properties of 2.54 mm and 0.6 mm thick 347H by 650°C-1000h (a) vacuum exposure and (b) DF4 exposure.

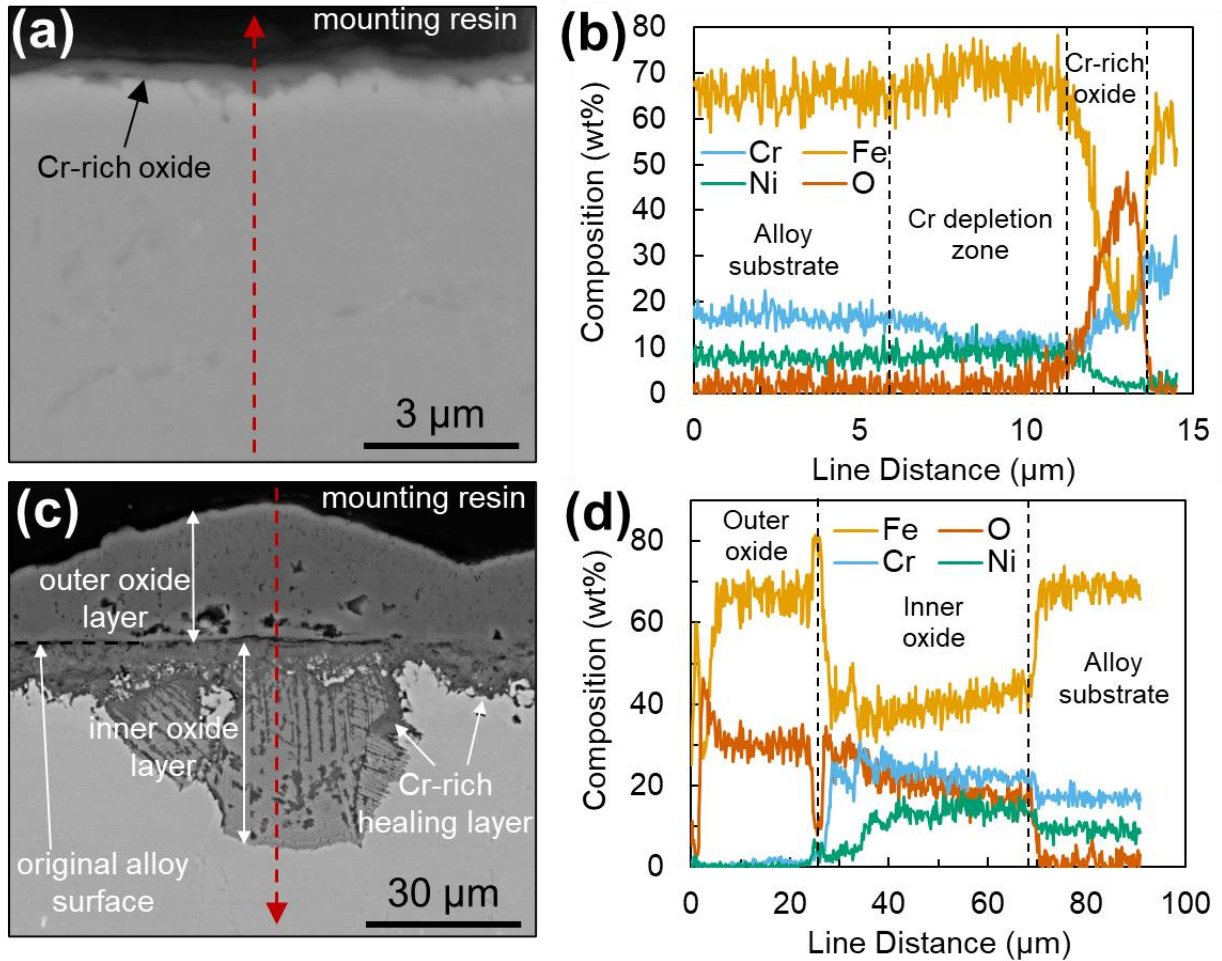


Fig. 5 Cross-sectional analysis of the oxidized surface of DF4-exposed 2.54 mm thick 347H showing (a) BSE image and corresponding EDS line scan (taken along the red dashed line) for a typical region which formed a thin oxide layer (c-d) the same analysis for an atypical region which formed a thick oxide layer.

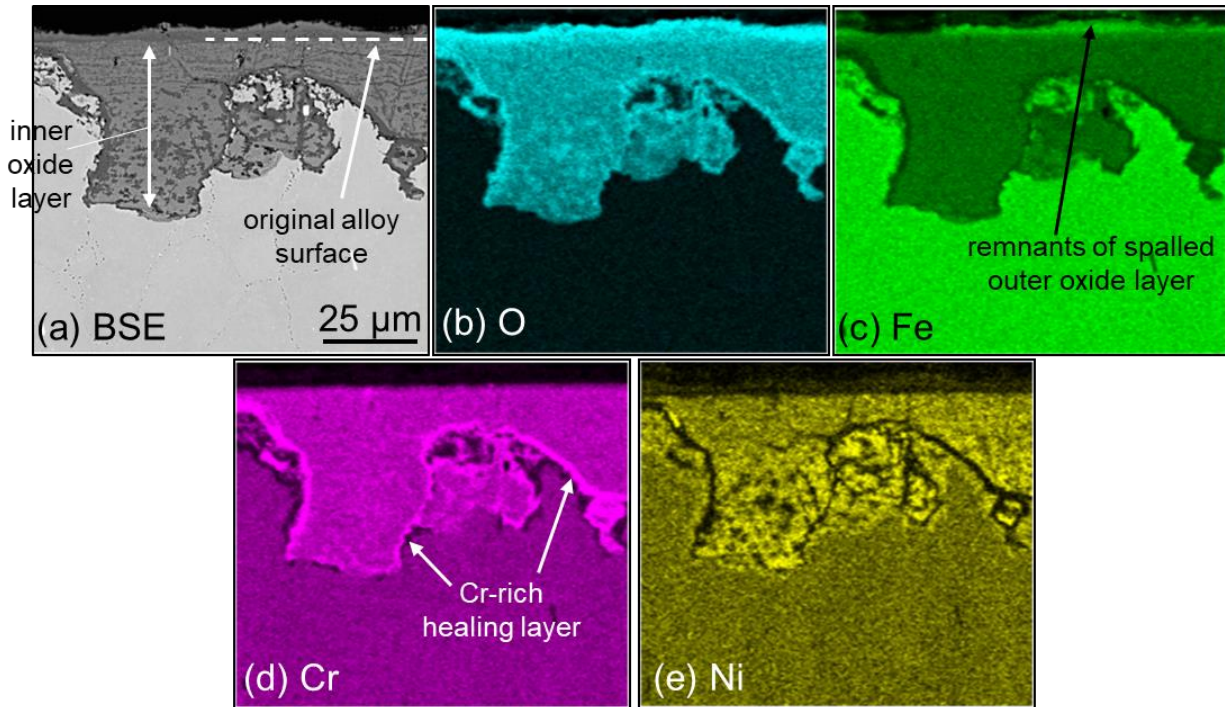


Fig. 6 Cross-sectional analysis of the oxidized surface of DF4-exposed 0.6 mm thick 347H showing (a) BSE image and (b-e) corresponding EDS maps.

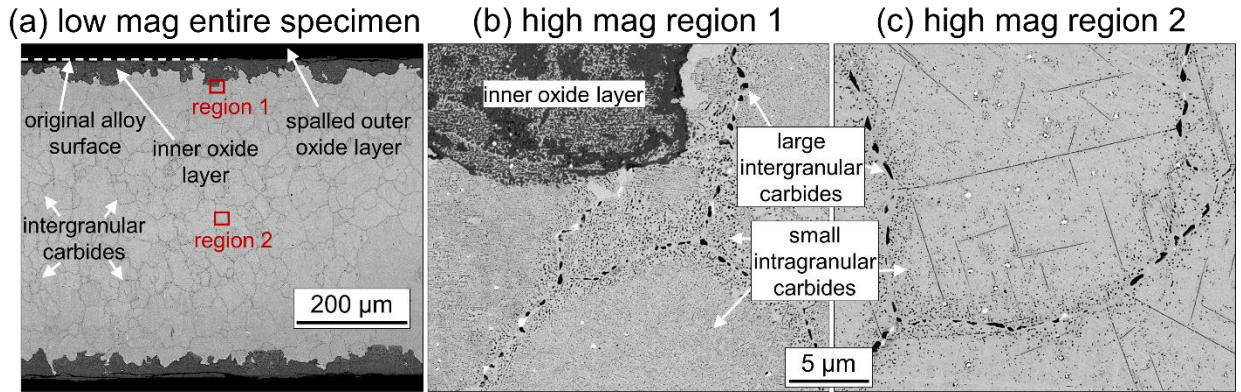


Fig. 7 Cross-sectional SEM images of DF4-exposed 0.6 mm thick 347H after etching to reveal metal carbides. (a) low magnification image showing the entire specimen (b-c) higher magnification images of the regions indicated in (a).

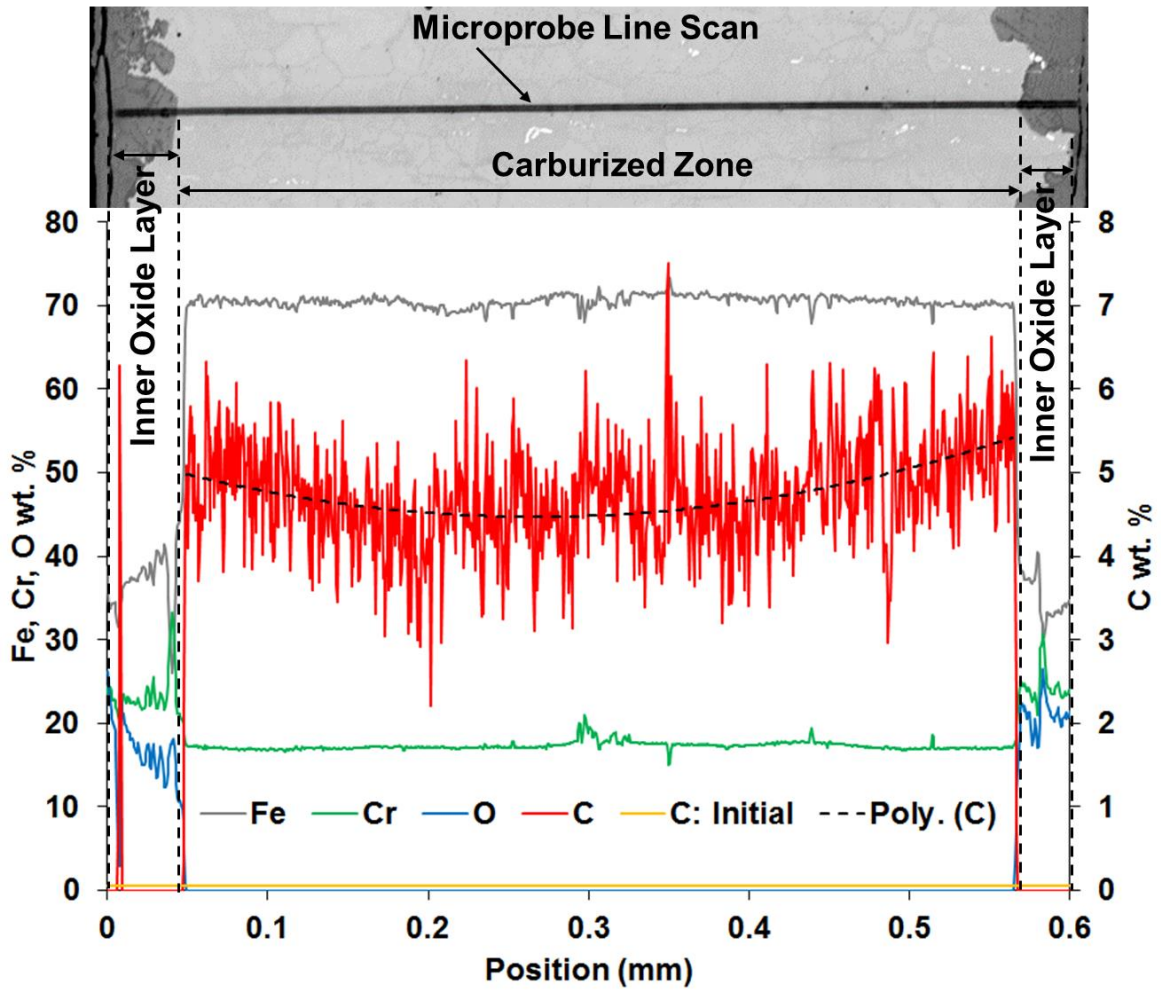


Fig. 8 EPMA line scan taken along the cross-section of DF4-exposed 0.6 mm thick 347H.

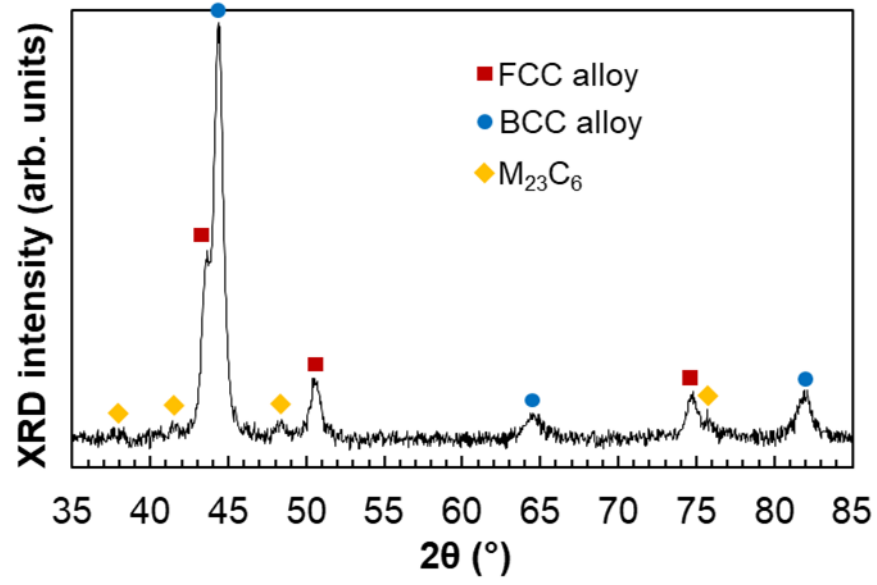


Fig. 9 XRD of DF4-exposed 0.6 mm thick 347H alloy substrate.

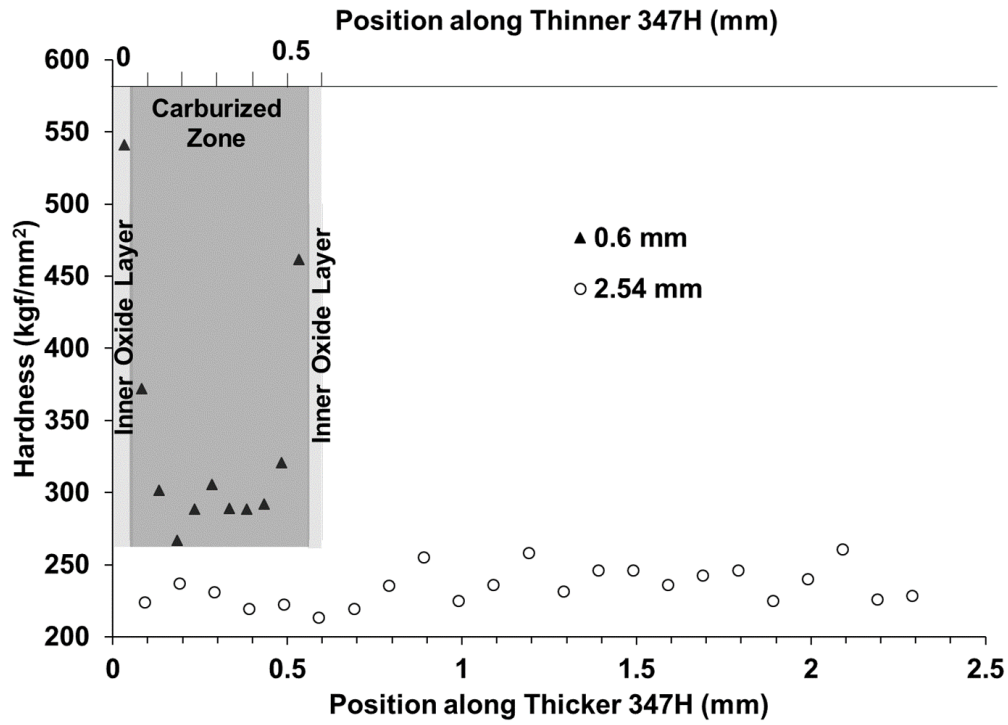


Fig. 10 Hardness profiles along cross-sections of 650°C-1000h DF4-exposed 0.6 mm and 2.54 mm thick 347 specimens.

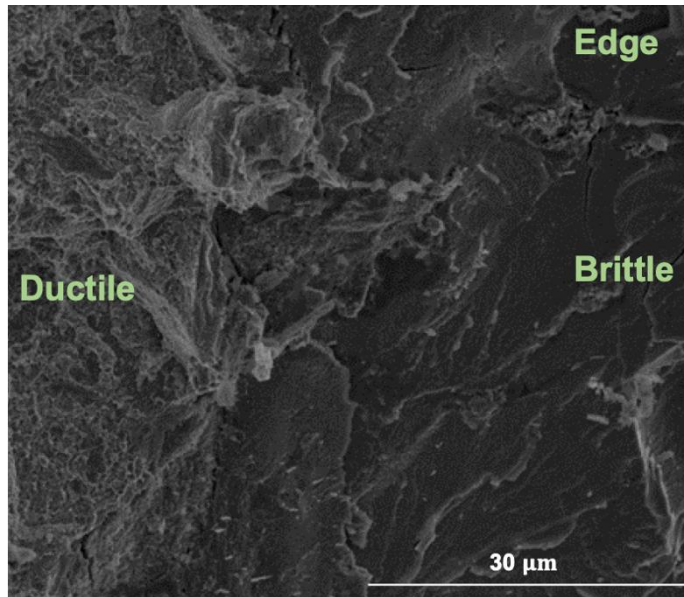


Fig. 11 SEM image of tensile fracture surface of a DF4-exposed 0.6 mm thick 347H.

Table 1 Composition of 347H steel in weight percent and balance is Fe.

Metal	Cr	C	Mn	P	S	Cu	Si	Ni	Mo	Ti	Al	N	Nb
347H	17.3	0.05	1.5	0.034	0.001	0.43	0.38	9.09	0.41	0.005	0.007	0.04	0.62

Table 2 Mechanical properties obtained from room temperature tensile testing on 347H.
 Each data represents the average of three test results with \pm one standard deviation.

Thickness (mm)	As-received or Exposed to 650°C-1000h	0.2% Yield Stress (MPa)	UTS (MPa)	% Area Reduction (Ductility)	Toughness (MJ/m³)
2.54	As-received	230 \pm 5	661 \pm 3	63 \pm 3	496 \pm 47
	Vacuum	258 \pm 5	660 \pm 1	62 \pm 4	527 \pm 18
	DF4	257 \pm 5	661 \pm 9	65 \pm 4	531 \pm 14
0.6	As-received	235 \pm 4	669 \pm 20	52 \pm 3	356 \pm 33
	Vacuum	243 \pm 6	632 \pm 18	54 \pm 1	282 \pm 9
	DF4	486 \pm 107	782 \pm 26	5.7	38